Uranyl Speciation in the Presence of Specific Ion Gradients at the Electrolyte/Organic Interface

Nitesh Kumar,[*,†] Michael J. Servis,[†] and Aurora E. Clark[*,†,‡]

†*Department of Chemistry, Washington State University, Pullman, Washington 99164, United States*

‡*Pacific Northwest National Laboratory, Richland, Washington 99354, United States.*

E-mail: nitesh.kumar@wsu.edu; auclark@wsu.edu

Abstract

Uranyl (UO_2^{2+}) speciation at the liquid/liquid interface is an essential aspect of the mechanism that underlies its extraction as part of spent nuclear fuel reprocessing schemes and environmental remediation of contaminated legacy waste sites. Of particular importance is a detailed perspective of how changing ion concentrations at the liquid interface alter the distribution of hydrated uranyl ion and its interactions with complexing electrolyte counterions relative to the bulk aqueous solution. In this work, classical molecular dynamics simulations have examined uranyl in bulk $LiNO_{3(aq)}$ and in the presence of a hexane interface. UO_2^{2+} is observed to have both direct coordination with NO_3^- and outer-sphere interactions via solvent-separated ion-pairing (SSIP), whereas the interaction of Li^+ with NO_3^- (if it occurs) is predominantly as a contact ion-pair (CIP). The variability of uranyl interactions with nitrate is hypothesized to prevent dehydration of uranyl at the interface, and as such the cation concentration is unperturbed in the interfacial region. However, Li^+ loses waters of solvation when it is present in the interfacial region, an unfavorable process that causes a Li^+ depletion region. Although significant perturbations to ion-ion interactions, solvation, and solvation dynamics are observed in the interfacial region, importantly, this does not change the association constants of uranyl with nitrate. Thus, the experimental association constants, in combination with knowledge of the interfacial ion concentrations, can be used to predict the distribution of interfacial uranyl nitrate complexes. The enhanced concentration of uranyl dinitrate at the interface, caused by excess adsorbed NO_3^-, is highly relevant to extractant ligand design principles as such nitrate complexes are the reactants in ligand complexation and extraction events.

1 Introduction

Chemical separation and purification of uranium, notably from aqueous solutions, is essential to various environmental[1–3] and industrial applications.[4] The highly stable U(VI) exists in the dioxo form, UO_2^{2+}, and can exhibit complicated speciation via complexation by solute anions including nitrate or carbonate. Nitric acid solutions are the most relevant to uranyl separations within the nuclear fuel cycle. Within solvent extraction processes that include Plutonium Uranium Reduction EXtraction (PUREX)[4,5] and Group ActiNide EXtraction (GANEX),[2] hydrated $UO_2(H_2O)_n^{2+}$ and uranyl nitrate complexes[6,7] are the reacting species with extracting ligands. The complexation reaction is presumed to occur at the aqueous/organic phase boundary, and thus the speciation of the metal ions at the interface is of significant importance.[8,9]

Although it is well-known that there may exist significant concentration gradients of solutes near the liquid/liquid interface,[10–13] how this perturbs the speciation of metal ions and their complexes relative to the bulk aqueous phase has not been the topic of significant study. An additional complication is that the heterogeneous environment of the liquid/liquid interface[14,15] may lead to a broad ensemble of local chemical environments that have the potential to shift energetic preferences. In bulk nitric acid it is well-known that UO_2^{2+} is on average pentacoordinate and associates with nitrate anions to form $UO_2(H_2O)_m(NO_3)_n^{(2-n)+}$ where n + m = 5.[16] However the association is weak, as has been measured by a number of experimental methods (UV-Vis,[17,18] IR/ Raman[19] NMR,[20,21] EXAFS[22–24] and microcalorimetry[25]). In the case of the mononitrate complex ($n = 1$) the reported association constant (K_1) varies from 0.05 - 0.70, while the second association constant (K_2) for the formation of $UO_2(NO_3)_2$ is generally agreed to be much lower at 0.02 - 0.05 at 298 K, depending upon the experimental methodology. Density functional theory (DFT) studies have examined uranyl coordination and nitrate binding modes,[26–28] and identified bidentate (η^2) nitrate to be significantly more stable than monodentate (η^1) in the gas phase. In contrast, the free energy difference between η^2 and η^1 in solution is predicted to significantly decrease, such

that an approximate equal population of both coordination modes should be observed in the aqueous phase.[19,26,27] Despite the efficacy of DFT studies of isolated uranyl nitrate complexes,[21,27,29,30] such methods are not able to study the speciation, solvation, and complex ion-ion interactions that occur in bulk electrolytes near industrially relevant conditions, let alone their interfaces.

Molecular dynamics simulations have emerged as a powerful tool to study multi-component solutions and their interfaces, providing a molecular scale understanding of the complex correlations amongst local solution environments and dynamic equilibria between different chemical species. Yet the applicability of MD simulation is constrained by the fidelity of the potentials that define intra- and inter-molecular interactions. Several non-polarizable pairwise additive potentials have been developed for uranyl cation, and parameterized for aqueous and nitrate containing solutions under dilute conditions.[31–33] Unfortunately, as we demonstrate, at appreciable NO_3^- concentrations those models significantly over-predict the degree of uranyl nitrate association and lead to long-range correlations of uranyl nitrate complexes at modest ionic strength. This work begins by optimizing the interaction terms between UO_2^{2+} and NO_3^- using a electrostatic continuum-type correction (ECC). The optimized force fields reproduce the experimentally-determined uranyl nitrate association constants and associated speciation over a wide range of uranyl and nitrate concentrations within bulk $LiNO_{3(aq)}$. The electrolyte/hexane interfacial region is then examined at high ionic strength, where significant perturbations to ion hydration across solvation shells, ion-ion interactions, and the heterogeneity of the interface, all have the potential to alter the association constants of UO_2^{2+} and NO_3^- relative to the bulk. Changes to the association constants would significantly complicate prediction of uranyl speciation, and thus reactivity, at the interface.

Within the interfacial region, MD simulations predict ion-specific interfacial adsorption that leads to the formation of weak ion double layering, and generates distinct ion concentration gradients approaching the interface. The changing hydrogen bond network and ion

gradients significantly influence the water dynamics and organization, while having modest impact upon nitrate fluctuations in the primary coordination sphere of uranyl. Interestingly, a large affect of electrolyte concentration lies within the the timescales associated with species in the first coordination sphere of UO_2^{2+}, as well as its residence within the interfacial region. The timescales of solvent exchange and the residence time of UO_2^{2+} within the interface are comparable, and have a strong linear correlation with $LiNO_3$ concentration — slowing by 50%.

Li^+ exhibits a depleted concentration in the interface relative to the bulk because of the unfavorable tendency to shed waters of solvation. The stability of both solvent separated ion-pairs and uranyl nitrate complexes (with nitrate in the primary coordination sphere) are hypothesized to reduce the ability of the interface to perturb uranyl solvation. As such, the concentration of UO_2^{2+} is unaffected by the presence of the interface. The growth of uranyl dinitrate species is observed at the interface consistent with an interfacial excess of nitrate anions and Li^+ depletion. As such, the relative concentrations of uranyl, nitrate and all uranyl nitrate species are consistent with experimental nitrate association constants in the bulk for a given $[LiNO_3]$. Based upon these observations, we propose that the interfacial ion concentrations (from experiment or theory), in conjunction with the experimental nitrate association constants from the bulk, are likely suitable to predict uranyl speciation and subsequent reactivity at the liquid/liquid phase boundary.

2   Methodology

2.1   Simulation Configurations and Protocols

All atom molecular dynamics simulations were performed using the GROMACS 2016.2 software package[34] to study uranyl nitrate speciation in bulk $LiNO_{3(aq)}$ and $LiNO_{3(aq)}$/hexane under varying electrolyte concentrations. Initial system configurations were generated using Packmol,[35] with a unit cell size of 60 Å × 60 Å × 60 Å for the bulk simulations and 60 Å

$\times$ 60 Å $\times$ 180 Å for the electrolyte/hexane (simulation box set up provided in Figure S 1). Bulk simulations were performed with a series of concentrations presented in Table 1. These include a 0.05 M and 0.25 M UO_2^{2+} with background electrolyte $LiNO_3$ from 1 to 5 M so as to compare experimental studies by Suleimenov et al.[36] of uranyl in nitric acid solutions. To compare with prior data reported by Ye et. al.[37], additional simulations of 0.25 M UO_2^{2+} with HNO_3 were also performed. All electrolyte/hexane simulations were performed at 0.25 M UO_2^{2+} and 0.5 M NO_3^- as a function of $LiNO_3$ concentration from 1 - 5 M (Table 1).

Table 1: The compositions of the systems simulated in this study, presented as the number of molecules/ions present and the associated molarity, M.

Electrolyte Bulk				
H_2O		UO_2^{2+}	Li^+	NO_3^-
7055		7 (0.05 M)	130 (1.00 M)	144 (1.10 M)
6945		7 (0.05 M)	260 (2.00 M)	274 (2.10 M)
6754		7 (0.05 M)	390 (3.00 M)	404 (3.10 M)
6685		7 (0.05 M)	520 (4.00 M)	534 (4.10 M)
6555		7 (0.05 M)	650 (5.00 M)	664 (5.10 M)
7055		32 (0.25 M)	130 (1.00 M)	194 (1.50 M)
6945		32 (0.25 M)	260 (2.00 M)	324 (2.50 M)
6754		32 (0.25 M)	390 (3.00 M)	454 (3.50 M)
6685		32 (0.25 M)	520 (4.00 M)	584 (4.50 M)
6555		32 (0.25 M)	650 (5.00 M)	714 (5.50 M)
Electrolyte/Hexane				
H_2O	Hexane	UO_2^{2+}	Li^+	NO_3^-
7055	1977	32 (0.25 M)	130 (1.00 M)	194 (1.50 M)
6945	1977	32 (0.25 M)	260 (2.00 M)	324 (2.50 M)
6754	1977	32 (0.25 M)	390 (3.00 M)	454 (3.50 M)
6685	1977	32 (0.25 M)	520 (4.00 M)	584 (4.50 M)
6555	1977	32 (0.25 M)	650 (5.00 M)	714 (5.50 M)

Non-bonded interactions were modeled using Lennard-Jones and coulombic interactions. Lorentz-Berthelot mixing rules were used for obtaining combinations of σ and ϵ parameters. The UO_2^{2+} and Li^+ ions were modeled using Wipff et al.[38,39] and Joung et al.[40] force fields respectively, while the NO_3^- force fields are derived from from Ye et al.[41] and Benay and Wipff[32]. The UO_2^{2+} force field reproduces the experimentally observed hydration of 5 in the first solvation shell in bulk water,[8,38,42] whereas the Li^+ potential was parameterized to reproduce the experimental hydration free energies and ion hydration in the aqueous phase.[40,43]

The all-atom General Amber Force Field (GAFF)[44] were implemented for n-hexane, with modified Lennard-Jones parameters to reproduce the experimental density and enthalpy of vaporization as developed by Vo et al.[45–47] The UO_2^{2+}, Li^+, and NO_3^- atom charges were then scaled from 100% to 75% in 5% increments using ECC,[48] which is an indirect correction to account for solvent driven polarization effects on hydrated ions.[49] In this manner, the coulombic interaction were tuned to reproduce the experimentally determined equilibrium constants[18,36] for different uranyl nitrate species and ensure coordination numbers and nitrate denticity that are consistent with experimental studies and prior *ab-initio* studies.[26,28] As described in the Results and Discussion, the ECC of 90% was observed to best reproduce the experimental uranyl nitrate association constants under ionic strengths similar to Suleimenov et al.[36] and provide reasonable coordination environments. It was employed for all subsequent molecular dynamics simulations. The TIP3P water model[50] was used for the bulk and electrolyte/hexane systems. Optimised force field parameters are given in the Supplementary Information, Table S1.

All systems were first equilibrated in the isobaric-isothermal NPT ensemble for 40 ns using the Nose-Hoover thermostat[51] and Parrinello-Rahman barostat,[52] followed by isochoric-isothermal NVT ensemble for 10 ns. The simulations were performed at 298 K using periodic boundary conditions with a leap frog verlet integrator[53] using a time step Δt of 2 fs. PME (Particle-Mesh Ewald) summation[54] was used for long range electrostatic interactions. After equilibration, 30 ns production runs were performed in the NVT ensemble and used for data analyses. Sampling frequencies of the production run include 25 fs & 3 ps dump times depending upon the property of interest.

2.2   Data Analysis

The focus of this work is to understand the variations in uranyl speciation that result from significant changes to ion concentration and changes to solution structure at the interfaces of electrolytes with non-polar media, relative to the bulk electrolyte phase. Toward this

end, the macroscopic interfacial properties (interfacial tension and width) were examined alongside analyses that reveal the local structure—including the coordination environments, solvation structure, and molecular speciation. The dynamic properties of molecular interactions, obtained from the relevant time correlation functions, are also reported. Statistical errors were determined using standard deviation of the calculated quantity over the length of the sampled trajectory.

Interfacial Tension. The Kirkwood and Buff[55] pressure tensor method was used to calculate the interfacial tension, γ,[56] as an integral over the z dimension as

$$\gamma = \frac{1}{N_{int}} \int_0^{L_z} \frac{1}{2} \langle P_{zz} - \frac{1}{2}(P_{xx} + P_{yy}) \rangle dz. \qquad (1)$$

where L_z is the box length, N_{int} is the number of interfaces ($N_{int} = 2$ in Figure S1) and P_{zz}, P_{yy}, and P_{xx} are the diagonal components of the pressure tensor.

Local Structure and Speciation. Atom pair distribution functions were first used to examine inter-atomic distance correlations. These were compared to prior experimental and simulation data during force field validation. The composition of the primary coordination sphere about UO_2^{2+}, and the solvation environments about NO_3^- and Li^+ were determined from networks of inter-molecular interactions using the ChemNetworks software package.[57] Distance geometric criterion were employed to define edges between nodes represented by UO_2^{2+}, H_2O, NO_3^- and Li^+. These criterion were based upon the first minimum of the associated atom pair correlation functions of interest (including $U\cdots O_N$, $U\cdots N_N$, $U\cdots O_W$, $Li^+\cdots O_W$ etc. as shown in Figure S7). Geometric criterion are listed in Table S2. The distribution of denticities of nitrate complexation to uranyl was determined from the edge counts between $U\cdots O_N$.

Dynamic Properties. It is of interest to understand how the presence of the liquid/liquid interface may alter the dynamic behavior of water of solvation and ion-ion interactions. The time of interaction of H_2O as well as the NO_3^- in the primary coordination

sphere of UO_2^{2+} were calculated based upon a geometric cutoff r_{min}, that defines the interaction. The probability P(t) associated with the interaction at time t and t+ Δt is

$$P(t) = N(t, \Delta t)/ \sum_t N(t, \Delta t) \tag{2}$$

and the respective residence time[58] (τ) is,

$$\tau = \int_0^\infty tP(t)dt, \tag{3}$$

where $N(t, \Delta t)$ is the continuous time duration of molecule/ion in the solvation shell or primary coordination sphere about the reference molecule/ion.[59] Nitrate ions are observed to have $\sim 10 \times$ faster dynamic exchange between the primary coordination sphere of uranyl and the second solvation shell, relative to water. Fast dynamic properties have been previously been reported to be sensitive to the geometric cutoff employed to define primary and secondary regions about a solute. To investigate the sensitivity of the nitrate residence time about UO_2^{2+}, the dynamic correction procedure of Ozkanlar et al.[58] was employed to remove the transient breaking and formation of the interaction caused by the $U \cdots O_N$ distance cutoff. Within the correction procedure, a tolerance of 1 ps with average persistence value of 7 ps was used. The computed residence times of nitrate in the uranyl solvation shell without correction was found to be 10 ps, whereas the correction procedure yielded a very similar value of 12 ps.

Interfacial Slab and Identification of Truly Interfacial Molecules Analysis. To identify variations in speciation and solution structure in the interfacial region, two separate analyses were performed. First, a slab of the solution in the interfacial region was analyzed by taking a 10 Å increment in the z direction, consisting of 5 Å on either side of the Gibbs dividing surface of the water, defined as the z-axis position where the density of H_2O is half of its value in bulk. The speciation, ion concentrations, residence times, and other properties were calculated in each slab and then compared to the analogous metrics of

species present the instantaneous surface of the water. The Identification of Truly Interfacial Molecules (ITIM) algorithm[60,61] was employed to define the instantaneous surface of water and ions directly in contact with the organic phase, and for the comparison of the speciation and dynamic properties of the ions in the slabs vs. the instantaneous surface. The density of molecules in the instantaneous surface is fitted to a Gaussian function to obtain the position along z of the mean μ_0 of the distribution. The μ_0 is then used as a reference point ($\mu = 0$) in the interface to define interfacial crest regions (Figure S2) (where the molecular density in the z direction negative to μ (5 Å)) and the trough regions (in the positive direction relative to μ).

3 Results and Discussion

3.1 UO_2^{2+} in Bulk $LiNO_{3(aq)}$

Force Field Optimization. The force field parameters describing uranyl nitrate interactions have a significant impact on the associated association constants and long-range interactions between intact uranyl nitrate complexes. The literature has relied heavily upon force fields developed by Wipff and coworkers,[37–39,62] to simulate uranyl in water, low ionic strength electrolytes, and in contact with non-polar organic phases. In more recent work, Liu et al. optimized two new sets of uranyl parameters to reproduce experimentally observed structural and diffusion properties of bulk aqueous UO_2^{2+}.[31] For the study of uranyl speciation in electrolyte solutions, these parameters can be combined with a variety of force fields developed, including AMBER[8,33,38] or OPLS-AA.[62,63] Accurate modelling of HNO_3 requires acid/water auto-dissociation and charge transfer corrections in acidic media. Although it has been somewhat common to combine the existing UO_2^{2+} and NO_3^- potentials, their use in concentrated electrolyte conditions, where many-body solvation and polarization effects[42] can alter both structural and dynamic properties, has not been studied in detail.

Benchmarking the simulation protocol includes testing of the ability of the complete set

of all interaction parameters (the force field) to reproduce the experimental K_1 and K_2 for formation of uranyl-nitrate complexes. Toward this end, a [LiNO$_3$] dependent study is first performed, where the concentration of all species is used in conjunction with Equations S7 and S9 to yield simulated K_1 and K_2 values. As a starting point, we begin by using the parameters and solution conditions previously reported by Ye et al[37], but using LiNO$_3$ as shown in Figure 1. Referred to as the 100% ECC data, the the Wipff[8,32] and AMBER[32,41] force fields were employed to describe UO_2^{2+} and NO_3^-, respectively. At a LiNO$_3$ concentration of 3.0 M and UO_2^{2+} of 0.25 M, a significant concentration of over-coordinated uranyl environments are observed. Nearly 40% of all uranyl nitrate species are $UO_2(NO_3)_4^{2-}$, with $\sim$15% as $UO_2(NO_3)_2$ and $\sim$5% as $UO_2NO_3^+$. In the systems with classically modeled HNO$_3$ with 0.2715 M uranyl, Ye et al. reported overestimation of uranyl nitrate complexation and the presence of a significant amount of tri-nitrato complex generally not observed in experimental estimations.[37] When nitrate is bound, there is a $\sim$65% η^2 coordination whereas prior analysis of the relative energetics of η^2 vs. η^1 in solution indicated no significant thermodynamic preference.[19,26,27] Finally, extended organizations are observed in the form of loosely bound intact uranyl nitrate species that appear to be correlated with the presence of $UO_2(NO_3)_4^{2-}$ and $UO_2(NO_3)_5^{3-}$ as these species have bridging and electrostatic interactions with one another via H$_2$O, Li$^+$, and NO$_3^-$, as observed in the U-U RDF (Figure S3). Although this was noted within the simulation literature,[37,41,62] there lacks strong experimental evidence for such long-range correlations. In combination, these data preclude simple calculation of the equilibrium constants K_1 and K_2 because of the complex equilibria with higher-nitrate containing species and water or nitrate bridged multinuclear U-containing configurations. Indeed, using the experimentally measured K_1 and K_2 values of 0.12 and 0.04,[36] it would be predicted that $\sim$25% of all uranyl species would exist as the mononitrate, and only $\sim$8% as the dinitro-uranyl. Other $UO_2(H_2O)_m(NO_3)_n^{(2-n)+}$ with $n > 2$ should be present in minimal concentrations.

To address these issues the electrostatic continuum correction methodology was em-
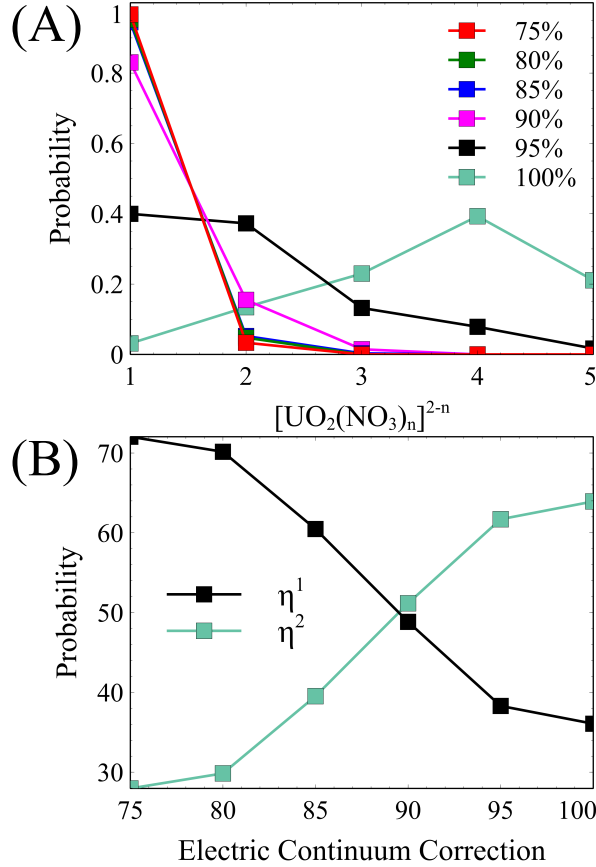
Figure 1: (A) Observed probabilities of uranyl nitrate complexes at various ECC values in 3 M LiNO$_3$ and 0.25 M UO$_2^{2+}$ (normalized to the entire concentration of all uranyl nitrate species). (B) Comparison of the probability of observing the η^1 vs. η^2 coordination modes of NO$_3^-$ to UO$_2^{2+}$ in 3 M LiNO$_3$ and and 0.25 M UO$_2^{2+}$ at various ECC values, with similar normalization. Note that 100% represents no charge scaling, 95% represents a 5% decrease in ion charges, and so on. The standard deviations are under 2% of the mean values.

ployed. This approach scales all ion charges and herein it is optimized to reproduce the experimentally observed equilibrium constants for the formation of the mono- and di-nitrato uranyl complexes. As cross-validation, the ligand denticity and solution organization as a function of $LiNO_3$ concentration was examined across all ECC values. As the speciation of uranyl-nitrate were examined (Figure 1A), the systematic scaling from 100% was observed to decrease the likelihood of highly coordinated uranyl ions by nitrate, effectively removing the equilibria of the $UO_2(NO_3)_4^{2-} \rightleftharpoons UO_2(NO_3)_3^-$ and the $UO_2(NO_3)_3^- \rightleftharpoons UO_2(NO_3)_2$, as well as the loosely organized aggregated species (as demonstrated Figure S3). At a charge scaling of 90% of the original value, the probabilities of over-coordinated uranyl species decreased significantly and loosely bound uranyl nitrate aggregates dissipated (Figure S3). At low $[LiNO_3]$ the purely aqueous solvation structure is unperturbed and remains $UO_2(H_2O)_5^{2+}$ at 1M $[LiNO_3]$. Bulk nitrate ion solvation is unperturbed, where at 1 M $LiNO_3$ the NO_3^- has on average 5.67 solvating H_2O with 11.56 HBs to H_2O, in good agreement with the nearly 12 hydrogen bonds in the bulk in prior work.[64] Similarly, the strongly hydrated Li^+ ions maintain an average hydration number of ~4.3 at 1 M $[LiNO_3]$, using a distance cutoff r_{min} of 3.0 Å in good agreement with the bulk aqueous phase.[65,66] Fitting the equilibrium constants K_1 and K_2 to the simulation data, using the equations S7 and S9 in the Supplementary Information, yields values of 0.12 and 0.04, respectively, which are well-within the range of experimental observation from spectroscopic measurements and are closest to the values of $K_1 = 0.15 \pm 0.04$ at 6.25 M ionic strength in a solution of $NaNO_3$ and $HClO_4$, and $K_1 = 0.11$ in $LiNO_{3(aq)}$.[18,19,36] In the system with 3 M $LiNO_3$, the η^2 and η^1 modes of uranyl nitrate coordination is observed at 52% and 48%, respectively (Figure 1B), which is in good agreement with prior *ab-initio* simulations and experimental studies that predicted nearly equal favorability of the two binding nodes in the solution phase.[19,26,27] Charge scaling greater than 10% leads to a significant weakening of the uranyl-nitrate interactions, and minimal concentration of any uranyl nitrate complexes and instead solvent separated ion-pair interactions, as demonstrated by the RDF in Figure S4. In combination,

these data indicate that the 90% ECC provides the best representation of uranyl-nitrate interactions in $LiNO_{3(aq)}$ across a range of concentrations. Using this optimized potential, the experimental K_1 and K_2 are well-reproduced, the ratio of mono- and bidentate NO_3^- binding modes are in agreement with *ab initio*[27] and experimental predictions,[19] and the solution structure as a whole is consistent with experimental observation.

$[LiNO_{3(aq)}]$ Dependent Changes to Uranyl Nitrate Speciation and Dynamics. The fraction of hydrated UO_2^{2+}, $UO_2(NO_3)^+$, $UO_2(NO_3)_2$ are plotted as a function of $[LiNO_3]$ and compared with analytical trends obtained from the experimental K_1 and K_2 in Figure 2. All other $UO_2^{2+}(NO_3^-)_m(H_2O)_n$ complexes are present in minor mole fractions (<0.05) throughout the concentration dependent study. For all $UO_2(NO_3)^+$ molecules, the percent observation of η^1 and η^2 binding modes are nearly equal at 1 M $[LiNO_3]$, and these ratios are consistent across all $[LiNO_3]$ concentrations. Among the three different binding modes of $UO_2(NO_3)_2$ (i.e. both monodentate, both bidentate, and one mono- and one bidentate) the mixed mono- and bidentate coordination mode is the most observed configuration (percentages provided in Table S4).

Ion solvation exhibits important dynamic properties, characterized by the exchange between first and second solvation shells on the ps to ns timescale.[67] These phenomena are intimately related to complexation reactions that occur via solvent dissociation pathways.[68,69] The residence times of solvating H_2O about uranyl are generally observed to be high, in the range 40-775 ps depending upon the simulation and experimental techniques, and solution conditions. Consider that NMR which has a distance dependent signal perturbation.[21,67,70] Although the distance at which NMR begins to measure the dynamic exchange of H_2O is not necessarily known, the computational residence time is generally defined as being strictly between the first and second solvation shells. Strong ion-dipole interactions of UO_2^{2+} with water,[71] and polarization across solvation shells is largely responsible for the long residence times.[72] However, this may be perturbed by long-range competitive interactions with background electrolytes, changes to overall solution-phase dynamic properties,[73] and direct
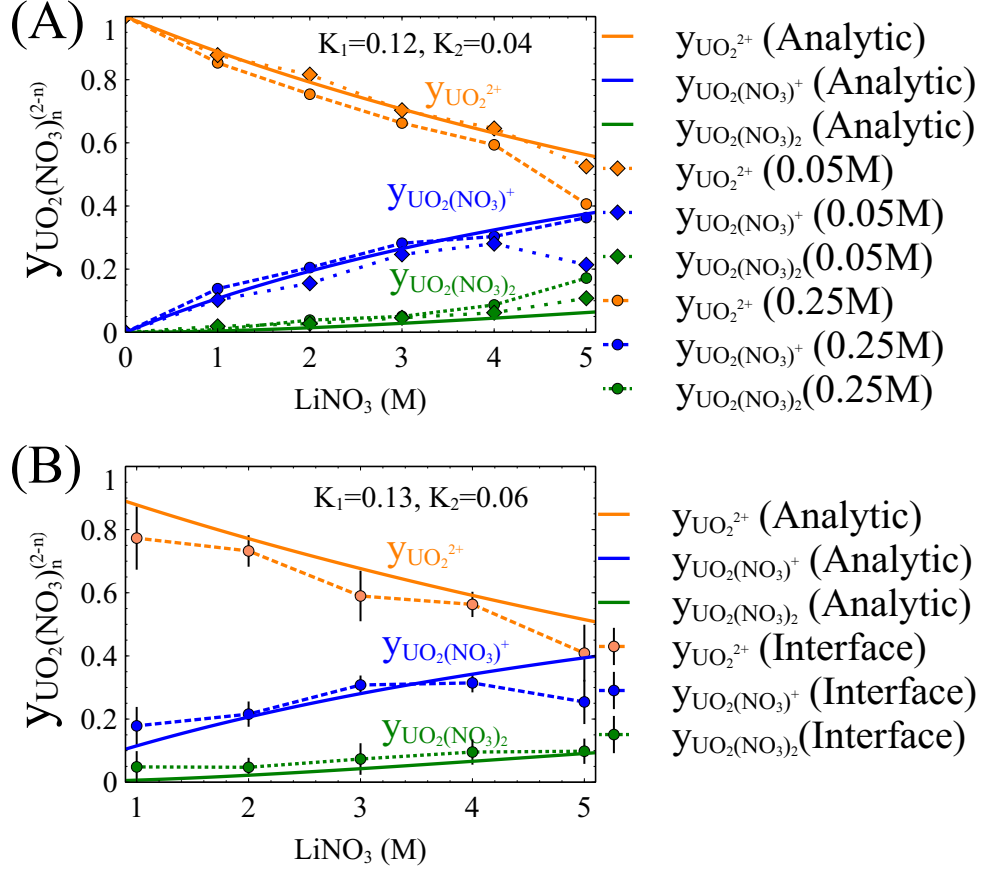
13

Figure 2: Variations in the mol fractions of uranyl nitrate complexes as a function of [LiNO$_3$] (in M) in (A) bulk [LiNO$_3$] for at 0.05 and 0.25 M UO$_2^{2+}$ and (B) Within the first 10 Å slab of the interfacial region of the electrolyte/hexane interface. The measured concentrations from the simulations have standard deviations less than 1% in the bulk and 2% within the interface, as indicated by the presented error bars. These data are presented in dashed lines, whereas the concentration variations expected from the experimental K$_1$ and K$_2$ values[36] are shown in bold solid lines.

ion-pairing or complexing ion interactions.[69]

As illustrated in Figure 3, the residence times of solvating H_2O about UO_2^{2+} ($\tau_{UO_2{}^{2+}-H_2O}$) linearly increases with [$LiNO_3$], irrespective of whether the solutions are 0.05 or 0.25 M UO_2^{2+}. The slope of a linear fit to the data is 53.01 and 40.49 with an $R^2 > 0.9$, indicating a strong linear dependence of the residence time of solvating water with the anion density in the second solvation shell of uranyl. In comparison to water, $NO_3{}^-$ residence in the primary coordination sphere ($\tau_{UO_2{}^{2+}-NO_3{}^-}$) is much smaller, ~ 10 ps at 1 M $LiNO_3$. The linear increase in $\tau_{UO_2{}^{2+}-NO_3{}^-}$ as a function of [$LiNO_3$] is only slightly larger than 1. In combination, the growth of uranyl nitrate species with increasing [$LiNO_3$] as well as concentration dependent perturbations to the organizational structure of the solution, do not immediately point to a source of the slowed-down hydration dynamics about UO_2^{2+}. On the one hand, the NO_3^- bound to UO_2^{2+} should decrease the electrostatic interaction of the cation with water and thus decrease the $\tau_{UO_2{}^{2+}-H_2O}$. However, recent work has indicated that the polarization of water by uranyl[71] is enhanced when non-hydrating solvent molecules have perturbed interactions caused by co-solvents.[73,74] In this vein, we first calculated the residence times of H_2O solvating NO_3^-, and of the H_2O-H_2O HB (hydrogen bond) lifetime (Figure S11). A net increase in residence time of solvating H_2O about NO_3^- was observed, while the H_2O-H_2O HB dynamics remained nearly unaltered. Interestingly, the U-N RDF (Figure S7) indicates significant growth of UO_2^{2+} interactions with nitrate as a solvent separated ion-pair (SSIP) with increasing [$LiNO_3$]. Both the concentration of SSIP configurations and number of NO_3^- in the second shell of UO_2^{2+} increase significantly. We hypothesize that as H_2O becomes confined between UO_2^{2+} and $NO_3{}^-$ in the SSIP configuration and its ability to exchange either around uranyl or nitrate is significantly hampered, which leads to the observed trends in Figure 3. This is justified by the similar slopes of 1.5 for the water residence times about NO_3^- as well as the NO_3^- about UO_2^{2+}.
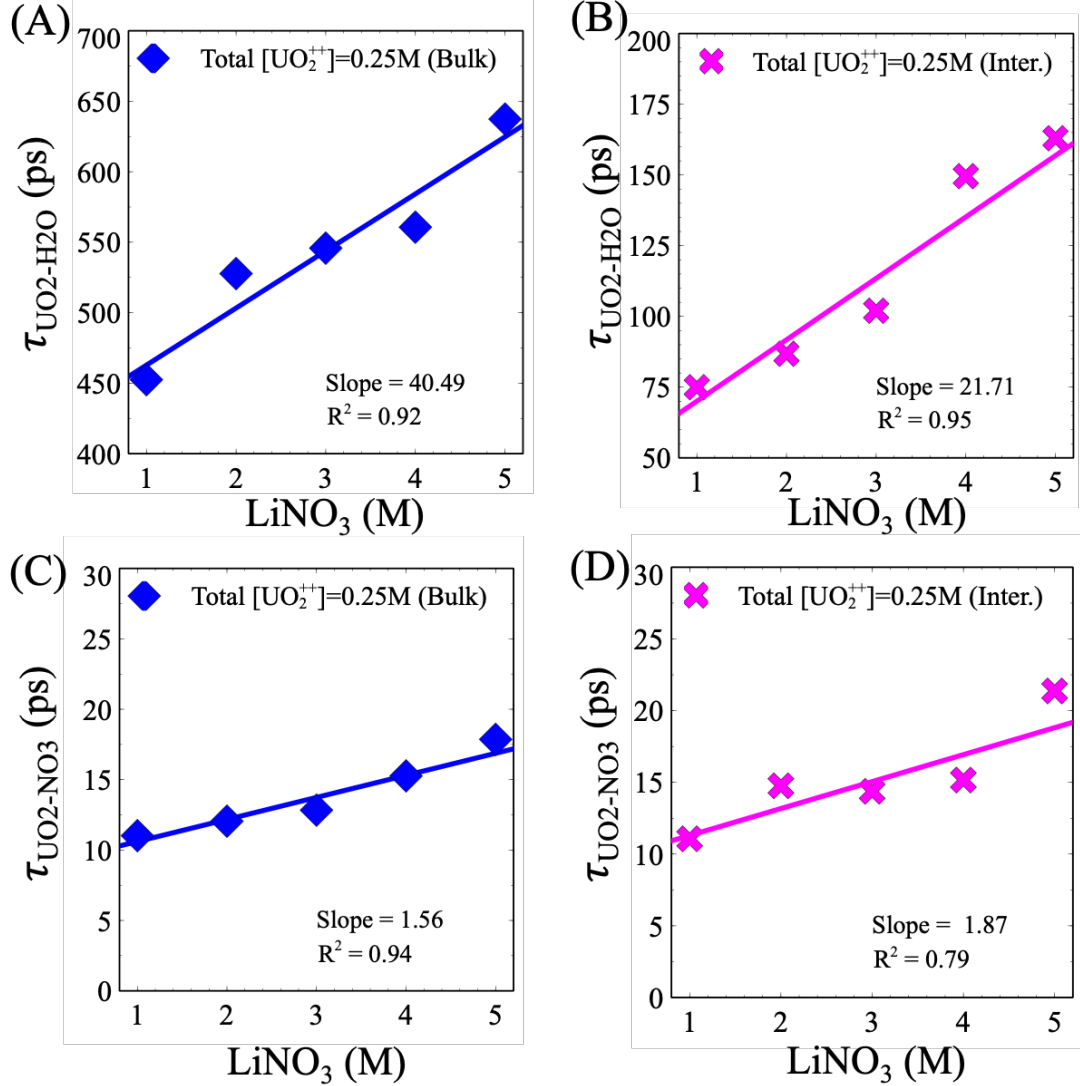
Figure 3: (A) Residence times of H_2O about UO_2^{2+} in bulk [LiNO$_3$]. (B) Residence times of H_2O about UO_2^{2+} in the first 10 Åslab of the electrolyte/hexane interface. (C) Residence times of NO_3^- about UO_2^{2+} in bulk [LiNO$_3$]. (D) Residence times of NO_3^- about UO_2^{2+} in the first 10Å slab of the electrolyte/hexane interface. The residence time curves are fitted to linear regression model. The slopes and R^2 values are shown in the insets. The standard errors are below 10 and 2 percent for nitrate and water, respectively.

3.2 Characteristics of UO_2^{2+} at the Electrolyte/Hexane Interface

The macroscopic and microscopic behavior of liquid/liquid interfaces are deeply intertwined. The interfacial tension (γ) increases nearly linearly with $LiNO_3$ concentration (Table S 3), in a manner consistent with the ion concentration at the electrolyte/hexane interface (Figure 4). The slope corresponding to the change in interfacial tension as a function of electrolyte concentration has been proposed to be a more accurate indicator of ion-specific effects[75,76] than an individual γ value at a specific concentration.[77] The average $d\gamma/dm$ of 1.69 $\pm$ 0.48 mN/mM (mili Newton per meter Molar) is in agreement with the experimental value of 1.23 $\pm$ 0.12 mN/mM for the analogous $LiNO_{3(aq)}$/vapor system.[77] We now consider the more in-depth molecular scale interfacial chemistry, with an emphasis upon understanding the concentration dependent speciation of uranyl in the interface relative to the bulk.

Ion Concentration Gradients. It is well-known that ions that reside at the interface perturb molecular-scale behavior as they introduce competitive interactions within an already altered environment relative to the bulk solution. Background electrolytes have been shown to influence metal-ligand chelation and speciation, as well as the rate determining steps in reaction kinetics. These may in turn influence mass-transfer kinetics across liquid interfaces.[68] A standard method to understand the ion concentration approaching the interface is to plot the charge density profiles (shown in Figure 4A). The charge densities as a function of concentration for UO_2^{2+}, NO_3^- and Li^+ are plotted relative to the position of the mean of the water densities (μ_0) present in the truly interfacial water layer. The figure shows a sharp negative peak between 0 Å and -5 Å and a positive peak between 0 Å and 5 Å. Collectively, this indicates a weak electric double layer structuring at the liquid/liquid interface. To further understand the distribution of ions in various interfacial regions (the crest and trough) we plotted the number density distribution of ions in the truly interfacial layer (Figure 4B–D) and present the percent distribution of all ions in the truly interfacial layer (layer 1) and subjacent layers in Table 2. The distribution of ions along μ axis reveals that both UO_2^{2+} and NO_3^- predominantly reside in the trough region (positive μ) whereas the
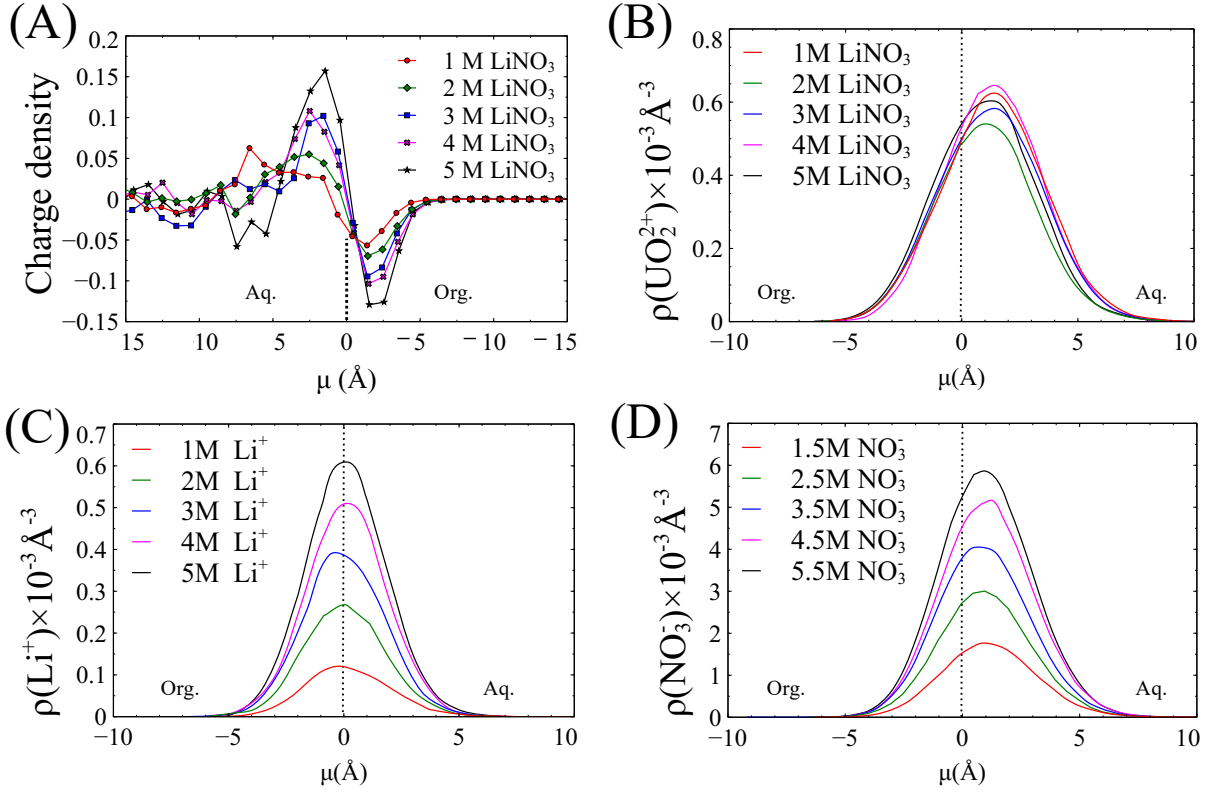
17

Figure 4: (A) Ion charge densities along μ-axis at various electrolyte concentrations in electrolyte/hexane systems (where $\mu = 0$ is the distance of the mean of the H_2O distance in the instantaneous surface). Number densities of (B) UO_2^{2+} (C) Li^+ (D) NO_3^- at the electrolyte/hexane interface with increase in [$LiNO_3$] are also presented. A negative value in the μ axis represents the crest of the instantaneous surface, facing the organic phase, and positive values describe the trough region where the instantaneous surface faces the aqueous electrolyte phase.

number density of Li^+ is distributed evenly in the crest and trough regions of the truly inter-
facial layer. From the percentage of ions in the interfacial layer (Table 2) it is apparent that
very little Li^+ exists at the instantaneous surface, although there is significant population
within the interfacial region as demonstrated by the density profile. These data are consis-
tent with recent X-ray photo-electron spectroscopy interpretations of the prevalence of Li^+
in lithium iodide solutions at the electrolyte/vapor interface.[78] Prior work has demonstrated
that Li^+ sheds solvating H_2O within the instantaneous surface, which disfavors residence
therein.[61] When combined with observation of relatively consistent NO_3^- concentration in
the instantaneous surface and subjacent layers, the negative charge density in the region
directly contacting the organic phase is presumed to be an outcome of Li^+ cation depletion
in the instantaneous surface rather than anionic excess.

Table 2: The percent distribution of ions in various interfacial layers at the electrolyte/hexane
per interface.

Interfacial Layer	NO_3^- (1.5 M)	Li^+ (1 M)	UO_2^{2+} (0.25 M)
1	5.35 ± 0.15	0.65 ± 0.45	5.35 ± 0.30
2	5.00 ± 0.05	4.70 ± 0.25	5.00 ± 0.40
3	5.45 ± 0.40	5.10 ± 0.30	5.45 ± 0.05
4	4.85 ± 0.40	5.20 ± 0.30	4.90 ± 0.05
5	4.95 ± 0.15	5.15 ± 0.05	4.95 ± 0.20
Interfacial Layer	NO_3^- (5.5 M)	Li^+ (5 M)	UO_2^{2+} (0.25 M)
1	4.45 ± 0.15	0.65 ± 0.15	4.85 ± 0.15
2	4.50 ± 0.15	4.80 ± 0.25	4.15 ± 0.40
3	5.20 ± 0.40	4.75 ± 0.10	4.45 ± 0.05
4	5.35 ± 0.05	4.75 ± 0.10	4.75 ± 0.10
5	5.40 ± 0.20	4.80 ± 0.35	5.05 ± 0.05

Ion Solvation and Ion-Ion Interactions. The solvation properties of ions within the
interfacial region were examined as a function of $[LiNO_3]$ and compared to the bulk solution.
As in prior work,[61] NO_3^- loses water of hydration at the electrolyte/hexane interface, a feature
that increases with $[LiNO_3]$. The average number of interfacial O_N-H_W HBs decreases from
11.18 at 1 M to 9.86 at 5 M $LiNO_3$ (Figure 5). Similarly, as $[LiNO_3]$ is increased, the limited
number of Li^+ also lose H_2O of solvation, from 4.24 at 1 M to 3.62 at 5 M $LiNO_3$ within the

first 10 Å slab of the interfacial region. Although the concentration of Li^+ is limited, the loss of H_2O with increase in $[LiNO_3]$ can be directly attributed to the result of ion-pairing, as demonstrated in Figure 5. The changes to nitrate solvation, in contrast, derive from both enhanced contact ion-pairing with Li^+ as well as changes to UO_2^{2+}, as described in more detail within the next section. Interestingly, when uranyl exists in its purely hydrated form at the interface, it does not lose any solvating water. The only observations of H_2O loss for UO_2^{2+} involve complexation with nitrate. The decrease in average interfacial uranyl hydration number (Figure 6) from 4.78 to 4.33 with increased $LiNO_3$ concentration is consistent with increase in uranyl nitrate species solely.
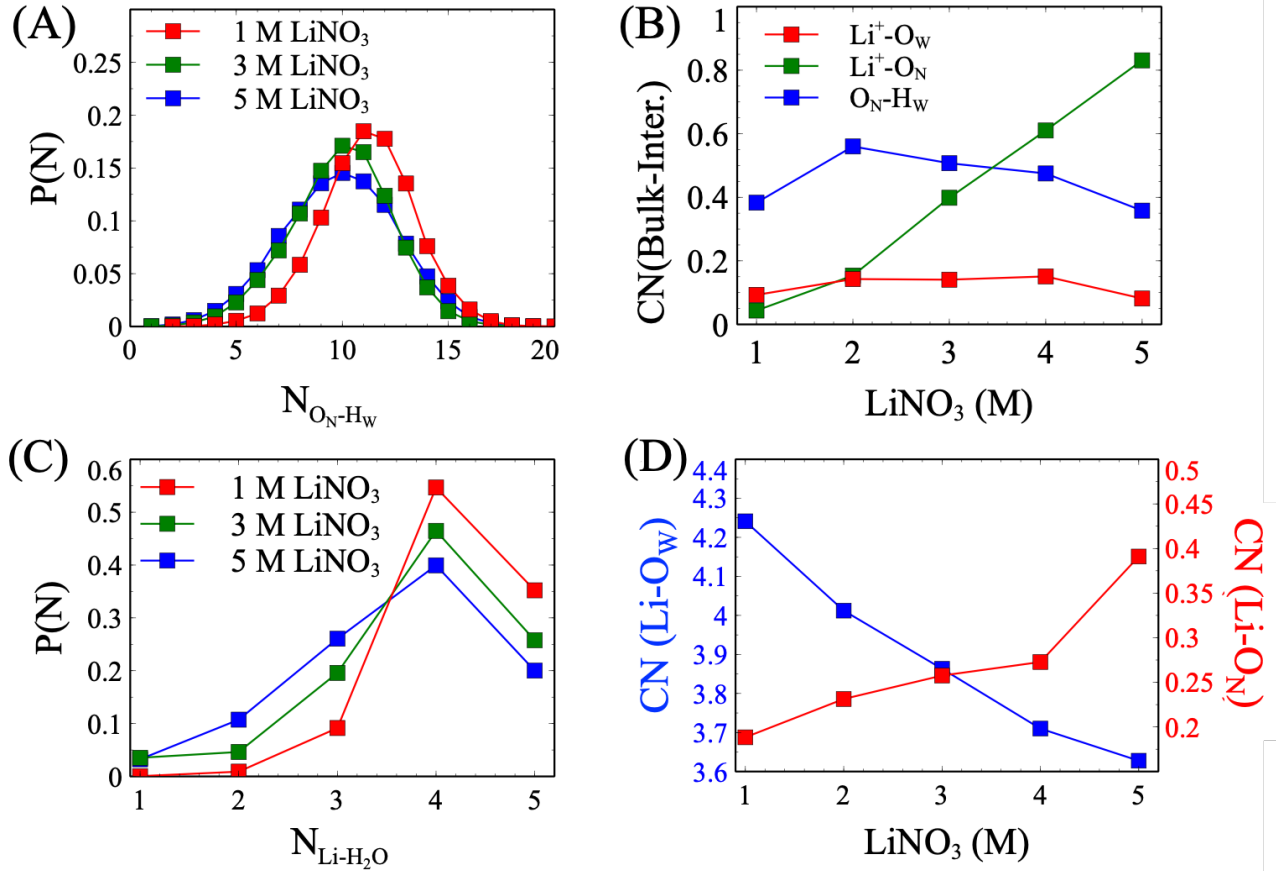

Figure 5: (A) $NO_3^-\cdots H_2O$ solvation distribution in truly interfacial layer at various $[LiNO_3]$. (B) Change in average interfacial $Li^+\cdots H_2O$, $Li^+\cdots NO_3^-$ and $NO_3^-\cdots H_2O$ interactions at electrolyte/hexane interface compared to bulk. (C) $Li^+\cdots H_2O$ coordination distribution in truly interfacial layer at various $[LiNO_3]$. (D) Variations in average $Li^+\cdots H_2O$ and $Li^+\cdots NO_3^-$ coordination in truly interfacial layer at various $[LiNO_3]$.

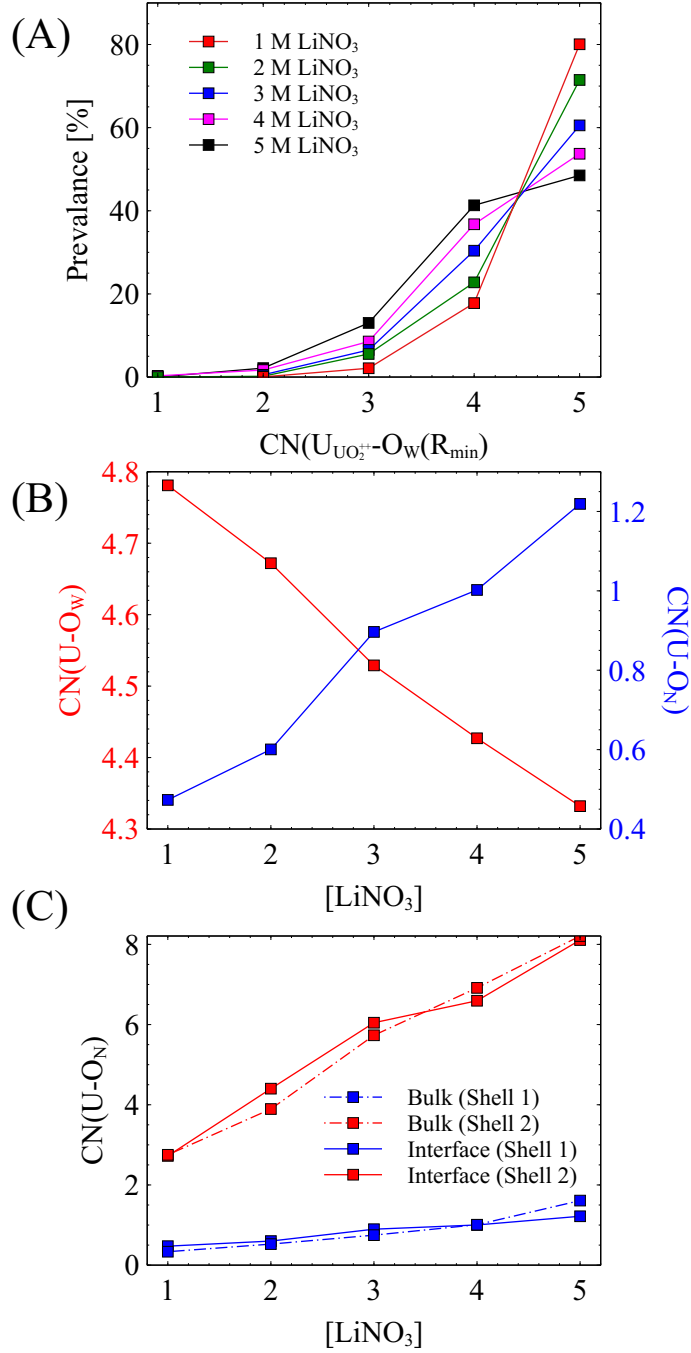Figure 6: (A) UO_2^{2+} coordination number (CN) distributions with water at the $LiNO_3$/hexane interface. (B) Variation in average interfacial $UO_2^{2+} \cdots H_2O$ CN (left axis) and average interfacial UO_2^{2+}-O(Nitrate) CN with $[LiNO_3]$. (C) Average CN of NO_3^- ions and in the first and second solvation shell of UO_2^{2+} with $[LiNO_3]$. All standard deviations are less than 2 percent.

Uranyl Nitrate Speciation. The interesting question then arises as to why UO_2^{2+} does not lose any H_2O of solvation within the interfacial region. Nitrate is observed to interact with uranyl in both primary and secondary solvation shells at the electrolyte/hexane interface, as shown in Figure 6C. Indeed, the SSIP form predominates. The concentration of SSIP uranyl-nitrate species is $\sim$5.5 times that of the complexed mononitrate species at 1 M and $\sim$6.5 times at 5 M compared in both the bulk and at liquid/liquid interface. The increase in nitrate solvation is observed to be nearly linear in both primary and secondary solvation shells, however the growth of SSIP interactions is significantly more steep.

Given the changes to the solvation properties of nitrate and uranyl in the interfacial region, and the introduction of competitive interactions at the interface, it is reasonable to question whether the nitrate association constants for uranyl would vary in the interfacial region relative to the bulk. The fractions of uranyl-nitrate complexes within the interfacial region of electrolyte/hexane (shown in Figure 2) reveal that the varying interfacial organization and ion concentrations do not perturb the uranyl-nitrate association constants relative to the bulk region. Within the interface, the mol fraction of $UO_2(NO_3)^+$ complex increases linearly from 0.17 $\pm$ 0.02 at 1 M to 0.25 $\pm$ 0.08 at 5 M [LiNO$_3$]. Even though the fraction of $UO_2(NO_3)_2$ complexes are less than $UO_2(NO_3)^+$ complexes, it also increases from 0.048 $\pm$ 0.004 at 1 M to 0.098 $\pm$ 0.003 at 5 M [LiNO$_3$]. The K_1 value of 0.13 and K_2 value of 0.06 are obtained by fitting to equations S7 and S9, respectively. A similar coordination behavior is observed in terms of percent denticity changes for all binding modes from 1 M - 5 M at the electrolyte/hexane interface compared to bulk.

Solvation Dynamics. Although the solvent exchange rate is typically considered a rate limiting process for metal-ligand complexation, when this reaction further depends upon residence in the interfacial region, then both the rate of solvent exchange and the rate of migration in and out of the interface, becomes highly important. Within the interface, the solvent exchange dynamics are significantly faster than in the bulk. At 1 M LiNO$_3$, the residence time of water is only a fifth of that in the bulk (75 ps vs. 450 ps). As such,

the timescales of H_2O exchange and residence times of UO_2^{2+} in the first 10 Å slab of the interface are comparable. As the [$LiNO_3$] increases, the solvation dynamics slows *and* the residence time in the interface both increase nearly linearly. The uranyl residence times at the electrolyte/hexane interface increased from 87 ps at 1 M to 180 ps at 5 M [$LiNO_3$], and in the latter the H_2O residence time about uranyl is 175 ps. Although the residence time of nitrate about uranyl also increases in the interfacial region, it is modest increase from ∼10 ps to ∼20 ps in going from 1 - 5 M $LiNO_3$. These data indicate that either aqueous exchange or ion residence times within the interfacial region may be the rate limiting factor for interfacial ligand complexation reactions, a topic that has not been significantly discussed within the literature.

Table 3: Residence times of uranyl ions in the interfacial region at electrolyte/hexane interface at various electrolyte concentrations.

$LiNO_3$ (M)	Residence Time τ (ps)
1	86.64
2	101.22
3	121.35
4	136.12
5	180.33

4 Conclusions

We present optimized force fields for the interaction of UO_2^{2+} in $LiNO_{3(aq)}$ that maintains accurate association constants for the formation of uranyl nitrate complexes over a 1 - 5 M electrolyte concentration regime. Under these conditions, the organization and dynamics of the bulk electrolyte solution was investigated. Subsequent biphasic simulation of the electrolyte/hexane system reveal several interesting features of the interfacial region. As anticipated based upon prior work, significant ion concentration gradients are observed for both Li^+ and NO_3^-, where depletion is observed for the former and excess is observed for the latter. Interestingly, the concentration of uranyl at the interface is the same as in the bulk, presumably because significant populations of solvent separated ion pairs with nitrate prevent uranyl dehydration therein. Second, the timescales of solvent exchange about uranyl are comparable to the residence time of the cation in the interfacial region. Thus, either of these processes may become the rate limiting step for interfacially mediated complexation reactions with extracting ligands. Both processes are also significantly slowed-down as [$LiNO_3$] is increased, nearly doubling over the 1 - 5 M regime. Finally, it is shown that despite significant changes to the interfacial organization and dynamics, the uranyl nitrate association constants are unperturbed. Therefore, the knowledge of ion concentration at the interface can be used to predict the changes to uranyl nitrate speciation and thus, the reacting species with extracting ligands like tributyl phosphate as part of the mechanism of solvent extraction.

Acknowledgement

References

(1) Katzin, L. I.; Sullivan, J. C. *The Journal of Physical Chemistry* **1951**, *55*, 346–374.

(2) Nash, K. L.; Choppin, G. R. *Separation Science and Technology* **1997**, *32*, 255–274.

(3) Nash, K. L.; Madic, C.; Mathur, J. N.; Lacquement, J. *The Chemistry of the Actinide and Transactinide Elements*; Springer, 2008; pp 2622–2798.

(4) Nash, K. L.; Lumetta, G. J. *Advanced Separation Techniques for Nuclear Fuel Reprocessing and Radioactive Waste Treatment*; Elsevier, 2011.

(5) Paiva, A.; Malik, P. *Journal of Radioanalytical and Nuclear Chemistry* **2004**, *261*, 485–496.

(6) Charbonnel, M.; Musikas, C. *Solvent Extraction and Ion Exchange* **1989**, *7*, 1007–1025.

(7) Condamines, N.; Musikas, C. *Solvent Extraction and Ion Exchange* **1992**, *10*, 69–100.

(8) Baaden, M.; Schurhammer, R.; Wipff, G. *The Journal of Physical Chemistry B* **2002**, *106*, 434–441.

(9) Kusaka, R.; Watanabe, M. *Physical Chemistry Chemical Physics* **2018**, *20*, 29588–29590.

(10) Jungwirth, P.; Winter, B. *Annu. Rev. Phys. Chem.* **2008**, *59*, 343–366.

(11) Chang, T.-M.; Dang, L. X. *Chemical Reviews* **2006**, *106*, 1305–1322.

(12) Vrbka, L.; Mucha, M.; Minofar, B.; Jungwirth, P.; Brown, E. C.; Tobias, D. J. *Current Opinion in Colloid & Interface Science* **2004**, *9*, 67–73.

(13) Luo, G.; Malkova, S.; Yoon, J.; Schultz, D. G.; Lin, B.; Meron, M.; Benjamin, I.; Vanỳsek, P.; Schlossman, M. L. *Science* **2006**, *311*, 216–218.

(14) Zhou, T.; McCue, A.; Ghadar, Y.; Bako, I.; Clark, A. E. *The Journal of Physical Chemistry B* **2017**, *121*, 9052–9062.

(15) Ghadar, Y.; Christensen, S. L.; Clark, A. E. *Fluid Phase Equilibria* **2016**, *407*, 126–134.

(16) Neuefeind, J.; Soderholm, L.; Skanthakumar, S. *The Journal of Physical Chemistry A* **2004**, *108*, 2733–2739.

(17) Marcantonatos, M.; Deschaux, M.; Celardin, F. *Chemical Physics Letters* **1980**, *69*, 144–150.

(18) Betts RH, M. R. *J Chem Soc* **1949**, *0*, S286–S294.

(19) Brooker, M.; Huang, C.-B.; Sylwestrowicz, J. *Journal of Inorganic and Nuclear Chemistry* **1980**, *42*, 1431–1440.

(20) Szabó, Z.; Glaser, J.; Grenthe, I. *Inorganic Chemistry* **1996**, *35*, 2036–2044.

(21) Farkas, I.; Bányai, I.; Szabó, Z.; Wahlgren, U.; Grenthe, I. *Inorganic Chemistry* **2000**, *39*, 799–805.

(22) Thompson, H. A.; Brown, G. E.; Parks, G. A. *American Mineralogist* **1997**, *82*, 483–496.

(23) Duvail, M.; Dumas, T.; Paquet, A.; Coste, A.; Berthon, L.; Guilbaud, P. *Physical Chemistry Chemical Physics* **2019**, *21*, 7894–7906.

(24) Ferru, G.; Gomes Rodrigues, D.; Berthon, L.; Diat, O.; Bauduin, P.; Guilbaud, P. *Angewandte Chemie International Edition* **2014**, *53*, 5346–5350.

(25) Rao, L.; Tian, G. *The Journal of Chemical Thermodynamics* **2008**, *40*, 1001–1006.

(26) Bühl, M.; Diss, R.; Wipff, G. *Inorganic Chemistry* **2007**, *46*, 5196–5206.

(27) Bühl, M.; Kabrede, H.; Diss, R.; Wipff, G. *Journal of the American Chemical Society* **2006**, *128*, 6357–6368.

(28) Bühl, M.; Diss, R.; Wipff, G. *Journal of the American Chemical Society* **2005**, *127*, 13506–13507.

(29) Bühl, M.; Schreckenbach, G.; Sieffert, N.; Wipff, G. *Inorganic Chemistry* **2009**, *48*, 9977–9979.

(30) Szabo, Z.; Grenthe, I. *Inorganic Chemistry* **1998**, *37*, 6214–6221.

(31) Kerisit, S.; Liu, C. *The Journal of Physical Chemistry A* **2013**, *117*, 6421–6432.

(32) Benay, G.; Wipff, G. *The Journal of Physical Chemistry B* **2014**, *118*, 3133–3149.

(33) Guilbaud, P.; Wipff, G. *Journal of Molecular Structure: THEOCHEM* **1996**, *366*, 55–63.

(34) Abraham, M.; Murtol, T.; Schulz, R.; Pall, S.; Smith, J.; Hess, B.; Lindhal, E. *SoftwareX* **2015**, *1-2*, 19–25.

(35) Martinez, L.; Andrade, R.; Birgin, E.; Martinez, J. *Journal of Computational Chemistry* **2009**, *30*, 2157–2164.

(36) Suleimenov, O.; Seward, T. M.; Hovey, J. *Journal of Solution Chemistry* **2007**, *36*, 1093–1102.

(37) Ye, X.; Smith, R. B.; Cui, S.; de Almeida, V.; Khomami, B. *Solvent Extraction and Ion Exchange* **2010**, *28*, 1–18.

(38) Guilbaud, P.; Wipff, G. *The Journal of Physical Chemistry* **1993**, *97*, 5685–5692.

(39) Baaden, M.; Burgard, M.; Wipff, G. *The Journal of Physical Chemistry B* **2001**, *105*, 11131–11141.

(40) Joung, I. S.; Cheatham III, T. E. *The Journal of Physical Chemistry B* **2008**, *112*, 9020–9041.

(41) Ye, X.; Cui, S.; de Almeida, V. F.; Hay, B. P.; Khomami, B. *Physical Chemistry Chemical Physics* **2010**, *12*, 15406–15409.

(42) Rai, N.; Tiwari, S. P.; Maginn, E. J. *The Journal of Physical Chemistry B* **2012**, *116*, 10885–10897.

(43) Burgess, J. *Metal Ions in Solution*; Halsted Press, 1978.

(44) Wang, J.; Wolf, R. M.; Caldwell, J. W.; Kollman, P. A.; Case, D. A. *Journal of Computational Chemistry* **2004**, *25*, 1157–1174.

(45) Vo, Q. N.; Hawkins, C. A.; Dang, L. X.; Nilsson, M.; Nguyen, H. D. *The Journal of Physical Chemistry B* **2015**, *119*, 1588–1597.

(46) Vo, Q. N.; Dang, L. X.; Nilsson, M.; Nguyen, H. D. *The Journal of Physical Chemistry B* **2016**, *120*, 6985–6994.

(47) Servis, M. J.; Clark, A. E. *Physical Chemistry Chemical Physics* **2019**, *21*, 2866–2874.

(48) Leontyev, I.; Stuchebrukhov, A. *The Journal of Chemical Physics* **2009**, *130*, 02B609.

(49) Kirby, B. J.; Jungwirth, P. *The Journal of Physical Chemistry Letters* **2019**, *10*, 7531–7536.

(50) Mark, P.; Nilsson, L. *The Journal of Physical Chemistry A* **2001**, *105*, 9954–9960.

(51) Evans, D. J.; Holian, B. L. *The Journal of Chemical Physics* **1985**, *83*, 4069–4074.

(52) Melchionna, S.; Ciccotti, G.; Lee Holian, B. *Molecular Physics* **1993**, *78*, 533–544.

(53) Van Gunsteren, W. F.; Berendsen, H. J. *Molecular Simulation* **1988**, *1*, 173–185.

(54) Essmann, U.; Perera, L.; Berkowitz, M. L.; Darden, T.; Lee, H.; Pedersen, L. G. *The Journal of Chemical Physics* **1995**, *103*, 8577–8593.

(55) Kirkwood, J. G.; Buff, F. P. *The Journal of Chemical Physics* **1949**, *17*, 338–343.

(56) Alejandre, J.; Tildesley, D. J.; Chapela, G. A. *The Journal of Chemical Physics* **1995**, *102*, 4574–4583.

(57) Ozkanlar, A.; Clark, A. E. *Journal of Computational Chemistry* **2014**, *35*, 495–505.

(58) Ozkanlar, A.; Zhou, T.; Clark, A. E. *The Journal of Chemical Physics* **2014**, *141*, 214107.

(59) Elola, M. D.; Ladanyi, B. M. *The Journal of Chemical Physics* **2006**, *125*, 184506.

(60) Pártay, L. B.; Hantal, G.; Jedlovszky, P.; Vincze, Á.; Horvai, G. *Journal of Computational Chemistry* **2008**, *29*, 945–956.

(61) Kumar, N.; Servis, M. J.; Liu, Z.; Clark, A. E. *The Journal of Physical Chemistry C* **2020**, *124*, 10924–10934.

(62) Sahu, P.; Ali, S. M.; Shenoy, K. T. *Physical Chemistry Chemical Physics* **2016**, *18*, 23769–23784.

(63) Jorgensen, W. L.; Maxwell, D. S.; Tirado-Rives, J. *Journal of the American Chemical Society* **1996**, *118*, 11225–11236.

(64) Smith, J. W.; Lam, R. K.; Shih, O.; Rizzuto, A. M.; Prendergast, D.; Saykally, R. J. *The Journal of Chemical Physics* **2015**, *143*, 084503.

(65) Mahler, J.; Persson, I. *Inorganic Chemistry* **2012**, *51*, 425–438.

(66) Benjamin, I. *Journal of Electroanalytical Chemistry* **2010**, *650*, 41–46.

(67) Tiwari, S. P.; Rai, N.; Maginn, E. J. *Physical Chemistry Chemical Physics* **2014**, *16*, 8060–8069.

(68) Knope, K. E.; Soderholm, L. *Chemical Reviews* **2013**, *113*, 944–994.

(69) Choppin, G. R. *Journal of Alloys and Compounds* **1997**, *249*, 9–13.

(70) Dang, L. X.; Vo, Q. N.; Nilsson, M.; Nguyen, H. D. *Chemical Physics Letters* **2017**, *671*, 58–62.

(71) Hemmingsen, L.; Amara, P.; Ansoborlo, E.; Field, M. J. *The Journal of Physical Chemistry A* **2000**, *104*, 4095–4101.

(72) Laage, D.; Hynes, J. T. *The Journal of Physical Chemistry B* **2008**, *112*, 7697–7701.

(73) Kelley, M. P.; Yang, P.; Clark, S. B.; Clark, A. E. *Inorganic Chemistry* **2018**, *57*, 10050–10058.

(74) Bühl, M.; Sieffert, N.; Chaumont, A.; Wipff, G. *Inorganic Chemistry* **2011**, *50*, 299–308.

(75) Collins, K. D.; Washabaugh, M. W. *Quarterly Reviews of Biophysics* **1985**, *18*, 323–422.

(76) Baldwin, R. L. *Biophysical journal* **1996**, *71*, 2056–2063.

(77) Pegram, L. M.; Record, M. T. *The Journal of Physical Chemistry B* **2007**, *111*, 5411–5417.

(78) Perrine, K. A.; Parry, K. M.; Stern, A. C.; Van Spyk, M. H.; Makowski, M. J.; Freites, J. A.; Winter, B.; Tobias, D. J.; Hemminger, J. C. *Proceedings of the National Academy of Sciences* **2017**, *114*, 13363–13368.